Available online at www.sciencedirect.com
ScienceDirect
International Journal of Heat and Mass Transfer 51 (2008) 823–834
International Journal of HEAT and MASS TRANSFER
www.elsevier.com/locate/ijhmt

An enthalpy method for modeling dendritic growth in a binary alloy

V.R. Voller

Saint Anthony Falls Laboratory, Civil Engineering, University of Minnesota, Mississippi River at 3rd Avenue SE, Minneapolis, MN 55414, USA

Received 20 November 2006; received in revised form 21 April 2007
Available online 27 June 2007

Abstract

An enthalpy fixed grid method is developed for modeling dendritic growth in an under-cooled binary alloy. The proposed numerical method couples explicit finite difference solutions of equations expressing the conservation of enthalpy and solute to an iterative procedure that enforces node by node consistency between enthalpy, solute, liquid fraction, and interface under-cooling. Calculations made with the scheme, are consistent with previously reported work, agree well with limit analytical solutions, approach the correct steady-state tip operating conditions, show grid size independence, are relatively free of grid anisotropy, and can be obtained with a low CPU cost.

Keywords: Dendritic growth; Enthalpy; Binary alloy; Under-cooling; Anisotropy

1. Introduction

If care is taken, it is possible to under-cool a liquid below its equilibrium solidification temperature. When a solid seed is placed in such an under-cooled melt, however, solidification will be initiated. Due to crystal anisotropy, or other perturbations in the system, the subsequent growth of the solid from the seed will not be uniform and an equiaxed dendritic crystal will form. The primary arms of the crystal will be aligned with the preferred growth directions. Stable growth of these arms is maintained through curvature and kinetic under-cooling of the solid–liquid interface.

Tracking the evolution of the solid–liquid interface of a crystal growing in an under-cooled melt is computationally challenging. A wide range of methods have been proposed in the literature [1–25]. The basic problem studied is the heat conduction controlled growth of a pure material, problems that involve fluid flow [3–6] and alloys [7–9] have also been studied. Very broadly speaking, methods based on standard numerical discretizations of the governing field equations can be split into two classes, Front Tracking Methods and Order Parameter Methods.

Front tracking methods can use deforming grids that evolve with the solid–liquid interface [10]. Typically, however, they employ field solutions on a fixed Eulerian background mesh and continuously reconstruct a Lagrangian description of the solid–liquid interface. This interface is tracked in time by explicitly satisfying suitable discrete forms of the interface heat balance condition. The reconstructed interface cuts through the elements of the background mesh and this information is used to modify the background field solution. This can be done by modification of the finite difference [5,11,12] or finite element approximations [8,13] in the vicinity of the interface, or through the distribution of interface heat sources [14].

Order parameter methods characterize the position of the interface by an order parameter $0 \leqslant \phi \leqslant 1$. A nodal value of $\phi_P = 0$ indicates the node point P is the solid, a value $\phi_P = 1$ indicates that P is in the liquid, and, a value $0 < \phi_P < 1$ indicates that P is in the vicinity of the solid–liquid interface. Values of the nodal order parameter are used to define a solidification heat source in the energy balance equation. They can also be used to evaluate interface

E-mail address: volle001@umn.edu

0017-9310/$ - see front matter © 2007 Elsevier Ltd. All rights reserved.
doi:10.1016/j.ijheatmasstransfer.2007.04.025

Nomenclature

C	concentration
C_0	initial concentration
c	volumetric specific heat (J/m^3 K)
D	mass diffusivity (m^2/s)
d_0	capillary length
f	liquid fraction
H	enthalpy (J/m^3)
K	thermal conductivity (J/m s K)
k	partition coefficient
L	cavity width
Le	Lewis number (α_l/D_l)
M	dimensionless liquidus slope
m	liquidus slope (K)
T	temperature (K)
T_f	fusion temperature (K)
T_m	equilibrium temperature (K)
t	time (s)
V	concentration potential
v	interface speed
W	interface width

Greek symbols

α, β	smear factors
α_l	liquid thermal diffusivity (m^2/s)
α_s	solid thermal diffusivity (m^2/s)
ϕ	order parameter
Δ	space step
ΔH	volumetric latent heat (J/m^3)
Δt	time step
ε	anisotropic strength
γ	surface tension (N/m)
κ	curvature (1/m)
λ	noise strength
μ	kinetic mobility (m/s K)
θ	interface angle

Subscripts

l	liquid value
s	solid value
P	node point
i, j	node point

Superscripts

+	liquid side of interface
−	solid side of interface
i	interface value

proprieties such as position and curvature. Typically the application of these methods requires differential equations to describe both the conservation of energy and the evolution of the order parameter. The key advantage of the approach is that calculations can be carried out on a fixed grid. Three popular order parameter methods are "level-set", "phase-field", and "enthalpy".

In level-set methods [15,16], the order parameter (level-set function) is usually defined as a distance function from the solid–liquid interface and is evolved with a pure advection transport equation. The velocity field for this advection is constructed to account for both the interface under-cooling and interface heat balance. In a similar fashion to front tracking approaches the level-set function is used to modify discretizations and source terms in the vicinity of the solid–liquid interface. In contrast to front tracking, however, the balance conditions on the interface are not explicitly satisfied, rather these conditions are implicitly accounted for through the update of the level-set function.

In phase-field methods [3,4,7,17–19] the physically sharp solid–liquid interface is modeled as a diffusive interface of finite width, W. To retain fidelity with the sharp-interface model this width should be chosen, according to the "thin-interface" analysis of Karma and Rappel [17], to be smaller than the microstructure morphology but larger than the capillary length scale d_0 ($\sim 10^{-9}$ m for metals) [7]. The order parameter is defined to vary smoothly across the interface and used to construct an energy functional that accounts for the interface under-cooling and heat balance. Then, through the minimization of the energy functional, an evolution differential equation for the order parameter is obtained. The accuracy of a numerical calculation of the phase-field equations requires that the grid size, in the vicinity of the interface, be at the scale of the interface width. Even with the "thin-interface" analysis [17] this could make calculations expensive; a situation that can be significantly relieved by employing dynamic adaptive gridding techniques [18].

There is an alternatively route to a phase-field evolution equation that does not require the minimization of an energy functional. In this approach, the order parameter is viewed as a "level-set" function and used to calculate expressions for the interface curvature and normal velocity; direct substitution of these expressions into the interface conditions results in an evolution equation for ϕ [19]. This concept of combining ideas between the phase-field and level-set methods is an emerging research theme, Tan and Zabaras [20] has utilized the concept of a diffuse interface in constructing a level-set method for dendritic growth and recently Sun and Beckermann [21] has uncovered extensive commonalities between the approaches.

Perhaps the most basic order parameter method is the well known enthalpy method. In this approach a single energy conservation equation for the entire solution domain, solid and liquid, is written in terms of the enthalpy

– the sum of sensible and latent heats. Solution can be made on a fixed space grid and the interface tracked by use of the liquid fraction f, a parameter that retains the feature of an order parameter, i.e., in the vicinity of the phase change $0 \leqslant f \leqslant 1$. The enthalpy method is successful at solving basic solidification problems where no under-coolings are present and the equilibrium solidification temperature is a fixed constant [26,27]. There is no reason, however, why this popular and relatively easy to use method can not be applied to solve problems of dendritic growth [6,9,22–25]. The first to try this was Tacke and co-workers [22,23] who employed an explicit finite difference discretization of the enthalpy equation, incorporating curvature under-cooling – the Gibbs–Thomson condition – through treating the liquid fraction as a level-set function. Tacke investigated the growth of an equiaxed crystal in an under-cooled pure melt under the condition of diffusion dominated heat transport. Recenly, Pal et al. [6] has extended the approach to account for a combination of advective-diffusive transport. This later work uses implicit time stepping and calculates the interface curvatures with methods form the cellular automata literature. Closely related work by Chatterjee and Charkraborty [25] combines the enthalpy method with lattice Boltzmann methods to simulate dendritic growth of a pure material in the presence of a flow field.

The work of Tacke and co-workers [22,23], Pal et al. [6], and Chatterjee and Charkraborty [25], clearly show the potential for using an enthalpy method for modeling dendritic growth. A drawback in the current enthalpy approaches however, is that the crystal anisotropy is not explicitly imposed; rather the anisotropy is implicitly controlled by the finite-difference grid. This means, on a standard two-dimensional finite-difference grid that crystal morphologies are restricted to fourfold symmetry and the primary arms are aligned with the grid axes. In addition, all the previously reported enthalpy dendritic models only consider pure melts. The objective of this paper is to further refine the enthalpy method for the modeling of dendritic growth. The key modifications are (1) an explicit specification of the crystal anisotropy, (2) extension to account for growth in both pure and binary alloy melts, and (3) the introduction of numerical devices that reduce the non-physical effect of grid anisotropy. Preliminary information on this modified approach has been presented in short conference proceedings [9,24]. This full paper provides an opportunity to detail a complete derivation and discussion of the approach, introduce new devices designed to reduce grid anisotropy, and present a comprehensive range of verification examples.

2. The sharp-interface model

An under-cooled binary alloy is contained in an insulated, two-dimensional, square cavity of side length L. Initially the alloy has a uniform concentration $C = C_0$ and temperature $T_u < T_m = T_f + mC_0$; T_m is the equilibrium temperature, T_f the fusion temperature of the pure solvent, and m is the (assumed linear) slope of the liquidus line. At time $t = 0$ a solid seed, that initiates solidification and crystal growth, is placed at the center of the cavity. For simplicity of development it will be assumed that there is no change in the volumetric specific heat c across the solid–liquid interface.

2.1. Thermal field

The thermal field is governed by the heat conduction equations

$$\frac{\partial T}{\partial t} = \nabla \cdot (\alpha_s \nabla T), \text{ in solid, and}$$
$$\frac{\partial T}{\partial t} = \nabla \cdot (\alpha_l \nabla T), \text{ in liquid} \quad (1)$$

where α is the thermal diffusivity and the subscripts s and l refer to the solid and liquid respectively. On the solid–liquid interface the heat balance gives

$$K_s \nabla T^- \cdot \mathbf{n} - K_l \nabla T^+ \cdot \mathbf{n} = \Delta H v \quad (2)$$

where $\mathbf{n}$ is the interface normal pointing into the liquid, ΔH is the volumetric latent heat, K is thermal conductivity, v is the interface speed in the normal direction, the superscript $-$ indicates evaluation on the solid side, and $+$ indicates evaluation on the liquid side.

2.2. Solutal field

The solutal field is governed by the diffusion equations

$$\frac{\partial C_s}{\partial t} = \nabla \cdot (D_s \nabla C_s), \text{ in solid, and}$$
$$\frac{\partial C_l}{\partial t} = \nabla \cdot (D_l \nabla C_l), \text{ in liquid} \quad (3)$$

where D is the mass diffusion. On the solid–liquid interface the partitioning of the solute gives

$$C_s = kC_l \quad (4)$$

where k is the partition coefficient, and the solute balance gives

$$D_s \nabla C_s \cdot \mathbf{n} - D_l \nabla C_l \cdot \mathbf{n} = C_l(1-k)v \quad (5)$$

2.3. Interface under-cooling

The equilibrium solidification temperature of the liquid alloy solidifies is $T_m = T_f + mC_0$. Due to the interface curvature and speed, and the solute partitioning and redistribution, however, the solid liquid interface is under-cooled to the temperature

$$T^i = T_m - \frac{\gamma(\theta)T_m}{\Delta H}\kappa - m(C_0 - C_l^i) - \frac{v}{\mu(\theta)} \quad (6)$$

where the superscript i indicates evaluation at the interface. The second term on the right of (6) is the Gibbs–Thomson

term accounting for decrease in interface free energy due to curvature; $\gamma(\theta)$ is the anisotropic surface tension, θ is the angle between the interface normal (pointing from solid to liquid) and the x-axis, and κ is the interface curvature (positive when the center of curvature is in the solid). The third term on the right of (6) accounts for the fact that, due to solute partitioning and transport, the liquid solute value at the interface will differ from the initial solute content of C_0; this term is referred to as the solutal under-cooling. The last term on the right of (6) is the kinetic under-cooling where $\mu(\theta)$ is the anisotropic kinetic mobility.

3. The enthalpy formulation – as a diffuse interface model

3.1. Derivation

Eqs. (1)–(6), referred to as the sharp-interface model, is the basis of front tracking methods for simulating dendritic growth. The distinct features are separate transport equations for the solid and liquid regions, (1) and (3), coupled through balance conditions, (2) and (5), applied at the sharp solid–liquid interface. In contrast, models based on an order parameter develop transport equations valid throughout the domain and implicitly capture the balance conditions through the evolution of the order parameter. In phase-field models [19] this is achieved through assigning a finite thickness to the solid–liquid interface across which variables and properties change smoothly. This concept of a diffuse interface can be used to arrive at an enthalpy based model of dendritic crystal growth. In this case the key property is a liquid fraction which changes smoothly across the interface, from $f=0$ in the solid to $f=1$ in the liquid. The liquid fraction takes the role of the order parameter and is used to develop smooth interpolations in variables and properties from the solid into the liquid. In this way, three new field variables are introduced. The volumetric enthalpy – the sum of sensible and latent heats – is defined as

$$H = cT + f\Delta H, \tag{7}$$

a mixture concentration is defined as

$$C = (1-f)C_s + fC_l, \tag{8}$$

and – following the initial idea of Crowley and Ockendon [28] – a concentration potential is defined as

$$V = \frac{C}{f(1-k)+k} \tag{9}$$

Further, in the diffusive interface, points that have a liquid fraction strictly in the range $0<f<1$, the liquid fraction is treated as a level-set function so that in calculating the interface temperature from (6) the curvature can be calculated as [29]

$$\kappa = \nabla\cdot\left(\frac{\nabla f}{|\nabla f|}\right) = \frac{f_y^2 f_{xx} - 2f_x f_y f_{xy} + f_x^2 f_{yy}}{(f_x^2+f_y^2)^{3/2}} \tag{10}$$

($f_x = \partial f/\partial x, f_{xy} = \partial^2 f/\partial x\partial y$, etc.), the normal velocity as [19]

$$v = -\frac{1}{|\nabla f|}\frac{\partial f}{\partial t} \tag{11}$$

and the interface orientation as

$$\theta = \tan^{-1}\left(\frac{f_x}{f_y}\right) \tag{12}$$

The definitions in (7)–(9) allow for a single domain formulation comprising equations for conservation of enthalpy

$$\frac{\partial H}{\partial t} = \nabla(K\nabla T) \tag{13}$$

where $K=(1-f)K_s + fK_l$ and the temperature is related to the enthalpy through

$$T = \begin{cases} \frac{\Delta H - L}{c}, & f=0 \\ T^i, & 0<f<1 \\ \frac{\Delta H}{c}, & f=1 \end{cases} \tag{14}$$

and conservation of solute

$$\frac{\partial C}{\partial t} = \nabla(D\nabla V) \tag{15}$$

where the potential V is related to the concentration C through (9) and $D=[k(1-f)D_s + fD_l]$. Note with the use of (8) and (9) in the solid ($f=0$) and in the liquid ($f=1$) domains (15) will reduce to sharp-interface diffusion equations given in (3).

Some comments are made.

1. In the development of the single domain equations the only requirement of the diffuse interface is to ensure a smooth continuity of variables and properties throughout the problem domain. In particular, the thickness of the interface has not been explicitly specified and, in fact, can be assumed to be arbitrarily small. This feature differs from phase-field models [3,4,7,17–19] and recent diffuse interface level-set methods[20] where the thickness of the interface is an explicit and key parameter entering in the governing equations.
2. In the limit of a vanishing interface thickness, the concentration potential $V^{(-)} \to V^{(+)}$, i.e., it has the same behavior as the temperature T.
3. Finally, for completeness it is noted that, although the convergence of the enthalpy formulation to the sharp-interface model under a vanishing interface thickness has been shown for the case of a pure material and no under-cooling, see Crank [27], a formal convergence treatment for the more general model is still open. In this work a rigorous convergence treatment is omitted but a demonstration that, in a one-dimensional domain, a numerical solution of the single domain system provides a close match to a recent analytical solution of the sharp-interface equations [30] is presented.

3.2. Dimensionless form

With the following dimensionless variables and scalings

$$T^* = \frac{T - T_f - mC_0}{\Delta H/c}, \quad C^* = \frac{C}{C_0}, \quad M = -\frac{cm}{\Delta H},$$
$$x^* = \frac{x}{d_0}, \quad t^* = \frac{\alpha_l t}{d_0^2}, \quad \kappa^* = d_0\kappa, \quad Le = \frac{\alpha_l}{D_l} \tag{16}$$

where the superscript (*) represent dimensionless variables and d_0 is the capillary length scale, the dimensionless form of the single domain equations are

$$\frac{\partial H^*}{\partial t^*} = \nabla^*(K^*\nabla^* T^*) \tag{17}$$
$$\frac{\partial C^*}{\partial t^*} = \nabla^*(D^*\nabla^* V^*) \tag{18}$$

where $\nabla^* \equiv \frac{\partial}{\partial x^*}, \frac{\partial}{\partial y^*}$. In these equations the appropriate dimensionless quantities and properties are defined as $H^* = T^* + f$, $C^* = fC_l^* + (1-f)C_s^*$, $V^* = \frac{C^*}{f(1-k)+k}$ $K^* = f + (1-f)\frac{\alpha_s}{\alpha_l}$ and $D^* = \frac{1}{Le}\left[f + k(1-f)\frac{D_s}{D_l}\right]$. Within the interface $0 < f < 1$ the dimensionless temperature, derived from (6) is given by

$$T^{i*} = -\kappa^*\frac{\mathrm{d}(\theta)}{\mathrm{d}_0} + MC_0(1-V^*) + \frac{c\alpha}{\Delta H\mu(\theta)d_0}\frac{1}{|\nabla^* f|}\frac{\partial f}{\partial t^*}, \quad 0 < f < 1 \tag{19}$$

where $\mathrm{d}(\theta) = \frac{\gamma(\theta)T_m c}{\Delta H^2}$ is the anisotropic capillary length. An often used fourfold symmetry model for this value is

$$\mathrm{d}(\theta) = \mathrm{d}_0(1 - 15\varepsilon\cos 4\theta) \tag{20}$$

where ε is the anisotropic strength.

4. Numerical solution of enthalpy formulation

4.1. The finite difference equations

In the following, a numerical solution is developed for Eqs. (17)–(20). The problem domain is a two-dimensional box with insulated sides. Initially the box contains an under-cooled liquid binary alloy and solidification is initiated by placing a solid seed at the equilibrium temperature at the center of the box. Due to symmetry, the problem domain will be restricted to the positive quadrant of the domain. Further, throughout the subsequent analysis, for simplicity of nomenclature, the $*$ superscripts, indicating a dimensionless quantity, will be omitted.

The domain is covered by a grid of square cell centered control volumes, see Fig. 1. Nodes are arranged in rows, numbered (bottom to top) $i = 1,\ldots,n$, and columns, numbered (left to right) $j = 1,\ldots,n$. The initial nodal setting is a fixed solute concentration C_0, a fixed under-cooling $T_u < 0$ and a liquid state ($f = 1$). The solution (growth of a dendrite) is initiated by setting the left hand corner node $(1,1)$ to a solid state ($f = 0$), a temperature $T = 0$, and concentration $C = kC_0$. In addition, a small amount of solid is placed in the immediate neighboring cells [$(1,2)$, $(2,1)$ and $(2,2)$] by reducing their nodal values to $f = 0.99$. This is sufficient to initiate the growth of a dendrite. Within a time step the calculation of this growth is as follows.

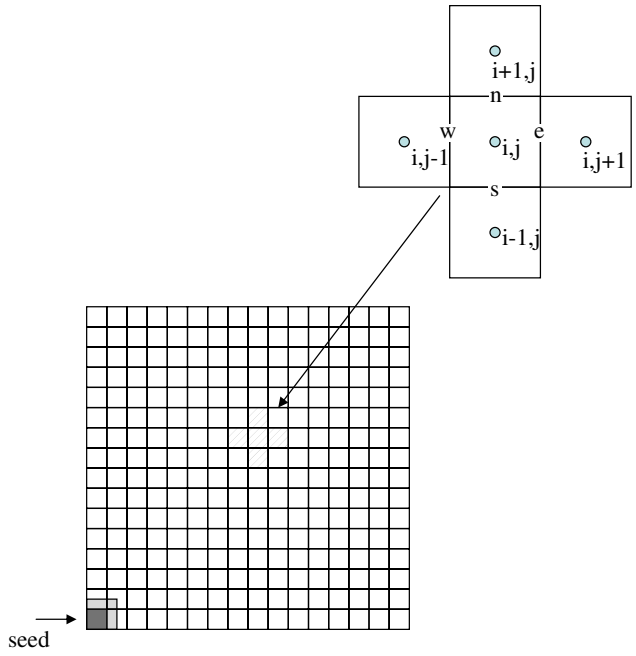

Fig. 1. Control volume and grid arrangement.

The fully explicit schemes of (17) and (18) are

$$H_{i,j}^{new} = H_{i,j} + \frac{\Delta t}{\Delta^2}[K_w(T_{i,j-1} - T_{i,j}) + K_s(T_{i-1,j} - T_{i,j}) + K_n(T_{i+1,j} - T_{i,j}) + K_e(T_{i,j+1} - T_{i,j})] \tag{21}$$

$$C_{i,j}^{new} = C_{i,j} + \frac{\Delta t}{\Delta^2}[K_w(V_{i,j-1} - V_{i,j}) + K_s(V_{i-1,j} - V_{i,j}) + K_n(V_{i+1,j} - V_{i,j}) + K_e(V_{i,j+1} - V_{i,j})] \tag{22}$$

where Δt is the time step, Δ is the space step, and the lower case subscripts w(est), e(ast), n(orth), and s(outh) indicate the face values for the control volume with center node (i,j). Note, unless otherwise stated, to ensure stability, the time step is set to $\Delta t = 0.1\Delta^2$. The values of the interface conductivities and diffusivities are calculated as $K_w = \left[\frac{f_{i,j-1}+f_{i,j}}{2} + \left(1 - \frac{f_{i,j-1}+f_{i,j}}{2}\right)\frac{\alpha_s}{\alpha_l}\right]$ and $D_w = \frac{1}{Le}\left[\frac{f_{i,j-1}+f_{i,j}}{2} + k\left(1 - \frac{f_{i,j-1}+f_{i,j}}{2}\right)\frac{D_s}{D_l}\right]$, etc. In all the results presented below, however, it is assumed that $\alpha_s = \alpha_l$ and $D_s = 0$, the Scheil assumption.

4.2. Solution in a time step

Eqs. (21) and (22) are solved (note no iteration is required) to update the nodal enthalpy and mixture concentration fields. The resulting fields are then used in a point by point iteration to extract the nodal values of V, T and f that are needed in the next time step. The steps in this iteration are as follows

1. With fixed values of new time nodal enthalpy $H^{\text{new}}_{i,j}$ and concentration $C^{\text{new}}_{i,j}$ in hand, the nodal field is swept.
2. If at node (i,j), the current value of the liquid fraction is strictly in the range $0 < f^r_{i,j} < 1$
   - the curvature κ, interface speed, and interface orientation θ are calculated from finite difference approximations of dimensionless versions of (10)–(12).
   - an approximation for the under-cooling T^i is obtained from (19)
   - the liquid fraction is updated as
   $$f^{r+1}_{i,j} = f^r_{i,j} + \omega(H^{\text{new}}_{i,j} - f^r_{i,j} - \Delta H) \tag{23}$$
   under the constraint that $f_{i,j}$ remains in the bounds $[0,1]$; the value $\omega \sim 0.5$ is an underrelaxtion.
   - the $r+1$ update for the temperature is calculated as $T^{\text{new}^{r+1}}_{i,j} = T^i$, and
   - the $r+1$ update for the concentration is $V^{\text{new}^{r+1}}_{i,j} = \frac{C^{\text{new}}_{i,j}}{f^{r+1}_{i,j}(1-k)+k}$.
3. If the current nodal liquid fraction is $f^r_{i,j} = 1$ or $f^r_{i,j} = 0$, step 2 is omitted and updates of the temperature $T^{\text{new}^{r+1}}_{i,j}$ and concentration potential $V^{\text{new}^{r+1}}_{i,j}$ are calculated directly from the definitions $H = T + f$ and $V = \frac{C}{f(1-k)+k}$ respectively.
4. The iterative sweeping ($r = 1,2,3,\ldots$) continues until a minimum number of iterations is exceeded ($r = 5$) and the largest nodal residual value $\text{res}_{i,j} = H^{\text{new}}_{i,j} - f^r_{i,j} - T^{\text{new}^r}_{i,j}$ falls below a tolerance (10^{-6} in the calculations reported here).

4.3. Advancing the solidification

Following the calculation of updated (new time level) T, V and f fields, there is one additional piece of bookkeeping that needs to be undertaken before calculations at the new time step can commence. The iterations outlined above are set up so that solidification in a given computational cell can only advance if the liquid in that cell is strictly $f_{i,j} < 1$. This requires that solidification be "seeded", at the appropriate time, in node volumes ahead of the advancing solid front. The appropriate time to switch is found by searching the nodal field, at the end of each time step, to locate nodes where solidification completed in the current step, i.e., nodes where $f_{i,j} > 0$ and $f^{\text{new}}_{i,j} = 0$. Then in each of the eight neighboring cells to node (i,j), if the current liquid fraction $f_{\text{nb}} > 1 - \delta$, where δ is a very small value ($\delta = 0.001$) indicating an essentially fully liquid state, its liquid value is updated to $f_{\text{nb}} = 1 - \delta$. The choice of the eight neighboring cells is important because it helps to suppress any grid anisotropy, see discussion below.

4.4. Remedial steps

The nature of the calculation outlined above will restrict the region where the liquid fraction is strictly in the limits $0 < f < 1$ to a band of the discrete domain which is on the order of one computational cell wide. Hence, although in the enthalpy formulation no explicit thickness of the interface is made, the practice creates a thickness that scales linearly with the grid size. This differs from level-set and phase-field methods, where the width of the interface band may include a number of computational cells. This "narrow band" feature of the enthalpy formulation can lead to problems in calculating interface properties from the nodal liquid fraction field, e.g., curvature [31]; problems that will not necessary be relieved by grid refinement since the thickness of the interface scales with the grid size. In this respect, an object of this paper is to introduce "ad-hoc" numerical devices that can lead to more reasonable calculations of interface curvature and direction from the thin band of interface information provide by an enthalpy model.

The narrow band problem can be relieved by "smearing" out its influence. One way this can be achieved is to use an extended finite difference stencil to calculate the liquid fraction derivatives used in the curvature (10), velocity (11) and direction (12) calculations. Finite difference approximations of the derivatives at node (i,j) are constructed to include nodal values from the eight nearest nodes. In this way derivatives in terms of single variable are approximated as

$$f_{x_{i,j}} = \frac{\alpha\frac{f_{i+1,j+1}-f_{i+1,j-1}}{2\Delta} + \frac{f_{i,j+1}-f_{i,j-1}}{2\Delta} + \alpha\frac{f_{i-1,j+1}-f_{i-1,j-1}}{2\Delta}}{1+2\alpha}, \ldots, \tag{24}$$

$$f_{yy_{i,j}} = \frac{\alpha\frac{f_{i+1,j-1}-2f_{i,j-1}+f_{i-1,j-1}}{\Delta^2} + \alpha\frac{f_{i+1,j}-2f_{i,j}+f_{i-1,j}}{\Delta^2} + \alpha\frac{f_{i+1,j+1}-2f_{i,j+1}+f_{i-1,j+1}}{\Delta^2}}{1+2\alpha}, \ldots, \tag{25}$$

where α is a user defined value. The cross derivative is calculated by the standard second order approximation

$$f_{xy_{i,j}} = \frac{f_{i+1,j+1} - f_{i+1,j-1}}{4\Delta^2} + \frac{f_{i-1,j-1} - f_{i-1,j+1}}{4\Delta^2} \tag{26}$$

If $\alpha = 0$, (24) and (25) give the standard second order approximations involving no more than two neighboring nodes. A stetting of $\alpha = 0.25$, used in this work, and consistent with Tacke [22], however, extends the approximation to all eight nearest neighbors.

Smearing can also be induced by constructing a weighted averaged liquid fraction field over the nearest neighboring cells

$$g_{i,j} = \left(1 - \sum_{\text{nb}} \beta_{\text{nb}}\right) f_{i,j} + \sum_{\text{nb}} \beta_{\text{nb}} f_{\text{nb}}, \tag{27}$$

subject to the conditions $\sum_{\text{nb}} \beta_{\text{nb}} = 1$, and $\beta_{\text{nb}} \geqslant 0$. It is emphasized and stressed that this construct is only used in calculating the front curvature, normal and velocity, in all other calculations the nodal liquid fraction $f_{i,j}$ must be used. In the current work, advantage is made of the fact that the crystal grows from the lower left to the upper right to invoke a simpler version of (27), viz.,

$$g_{i,j} = (1 - \beta) f_{i,j} + \beta f_{i+1,j+1} \tag{28}$$

5. Verification

5.1. Comparison with analytical solution

Under no curvature or kinetic under-cooling, a semi-infinite one-dimensional geometry, and boundary conditions $\frac{\partial C_s}{\partial x} = 0$, $\frac{\partial T}{\partial x} = 0$ at $x = 0$ and $C_l \to 1$, $T \to T_u < 0$ as $x \to \infty$, the sharp-interface model (1)–(6) admits an analytical similarity solution [30]. The similarity solution is realized through the fact that under the above conditions the values of the concentration C^i and temperature T^i at the interface remain constant through time. With this feature, the insulated condition at $x = 0$ immediately leads to the solid phase solutions $T = T^i$ and $C_s = kC^i$. From [30] temperature and concentration solutions in the liquid phase can be written as

$$T = T_u + (T^i - T_u)\frac{\operatorname{erfc}\left(\frac{x}{2\sqrt{t}}\right)}{\operatorname{erfc}(\lambda)} \tag{29}$$

$$C = 1 + (C^i - 1)\frac{\operatorname{erfc}\left(\frac{x\sqrt{Le}}{2\sqrt{t}}\right)}{\operatorname{erfc}\left(\lambda\sqrt{Le}\right)} \tag{30}$$

and the time dependent position of the planer solid–liquid interface written as

$$s = 2\lambda\sqrt{t} \tag{31}$$

The unknown values C^i, T^i and λ are found from the simultaneous solution of the equation of the under-cooling, the interface heat balance, and the interface mass balance

$$\begin{aligned} &T^i - MC_0(1 - C^i) = 0 \\ &\lambda\sqrt{\pi}e^{\lambda^2}\operatorname{erfc}(\lambda) - (T^i - T_u) = 0 \\ &(1-k)C^i\lambda\sqrt{Le}\sqrt{\pi}e^{\lambda^2 Le}\operatorname{erfc}(\lambda\sqrt{Le}) - (C^i - 1) = 0 \end{aligned} \tag{32}$$

Note the equivalence $V^i \equiv C^i$ at the solid–liquid interface.

Clearly the solution obtained form (29)–(32) cannot be used to check the treatment of the curvature and kinetic terms in the proposed enthalpy solution. It is an excellent vehicle, however, for checking two basic and critical features of the proposed scheme, viz., the solid reseeding treatment to advance the solidification and the single domain heat and solute transport treatment realized through the introduction of the enthalpy H and the concentration potential V. Fig. 2, compares predictions obtained with the proposed enthalpy method with the analytical solution for the case when $k = 0.1$, $MC_0 = 0.1$, $T_u = -0.5$, and $Le = 1.0$; a space step of $\Delta = 0.5$ and a time step of $\Delta t = 0.1$ is used. The agreement with profile and front movement predictions is excellent, in particular the front movement, recorded at every time step, is indistinguishable from the analytical solution. This result strongly indicates the mass and enthalpy conservation in the proposed approach.

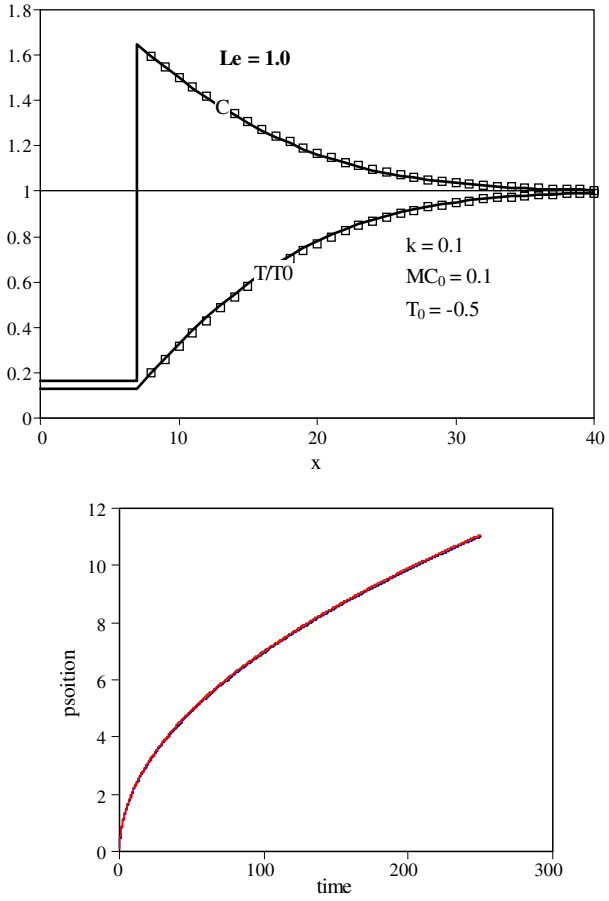

Fig. 2. Comparison between enthalpy and analytical solution for unidirectional solidification of a binary alloy.

5.2. Comparison with alternative models

Fig. 3 shows the enthalpy prediction for the equiaxed dendrite in pure material at dimensionless time $t = 37{,}000$ with initial under-cooling $T_u = -0.55$ and anisotropic strength $\varepsilon = 0.05$ in (20). In the calculation, a grid size of $\Delta = 2.5$ (1/4 box size 800×800) and a time step of $\Delta t = 0.625$ are used, the smearing parameters are set at as $\alpha = 0.25$ and $\beta = 0.25$ respectively, and a pure material is simulated by setting the partition coefficient $k = 0$. The conditions in Fig. 3 match those used by Kim et al. [16] to compare the predictive performance between phase-field and level-set methods. When compared with the results of Kim – Fig. 2 in Ref. [16] – a qualitatively close match can be observed between the enthalpy predictions and those obtained with the alternative models. The tip position and radius predictions are very close. The only noticeable discrepancy is at the roots of the dendrite arms; the enthalpy predictions show a slightly sharper curvature. The quality of the tip prediction is confirmed by noting that the dimensionless tip velocity approaches the steady-state velocity predicted with the microscopic solvability theory; see insert in Fig. 3 and more complete discussion on microscopic solvability below.

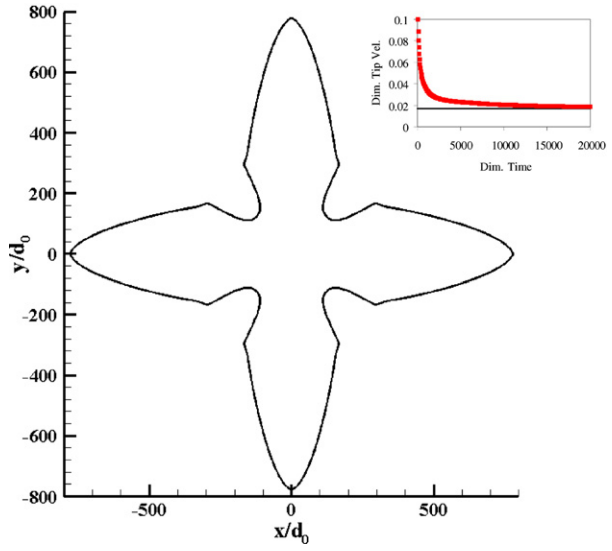

Fig. 3. Enthalpy predicted dendrite shape at $t = 37{,}000$, $T_u = -0.55$, $\varepsilon = 0.05$, $k = 0$, $\Delta = 2.5$ (1/4 box size 800 × 800) $\Delta t = 0.625$, $\alpha = 0.25$ and $\beta = 0.25$. Compare with Fig. 2 in ref [16]. Insert shows change of tip velocity with time.

5.3. A grid refinement study

An initial grid refinement analysis is made for a problem almost identical to the shown in Fig. 3; the difference is a larger under-cooling $T_u = -0.65$ and a simulation end time of $t = 6000$. Grid sizes from 4 to 2.5 in a 1/4 box size 400 × 400 are tested. For this, close to doubling of the grid size, the results, Fig. 4, are almost identical.

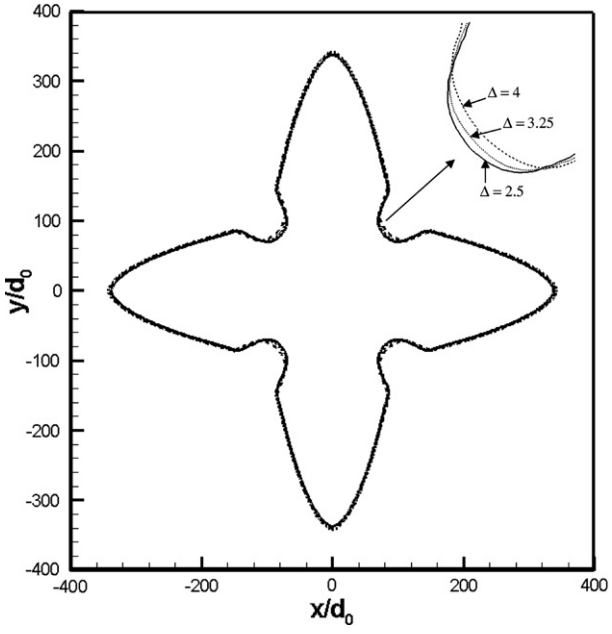

Fig. 4. Grid study. Enthalpy predicted dendrite shape at $t = 6{,}000$, $T_u = -0.65$, $\varepsilon = 0.05$, $k = 0$, $\alpha = 0.25$ and $\beta = 0.25$. Grid sizes of $\Delta = 2.5$, 3.25 and 4 in a 1/4 box size of 400 × 400 are compared.

5.4. Comparison with microscopic solvability theory

The growth of an equiaxed dendrite is driven by the thermal gradient in the liquid, decreasing in the direction of the normal. As a dendrite tip advances, its direction determined by the anisotropic surface tension ($\gamma\theta$), the value of the local thermal gradient increases accelerating the growth of the tip. This unstable behavior is offset by the fact that an advancing tip is associated with a larger value of curvature leading to a larger local under-cooling in the vicinity of the tip. In turn, the larger local under-cooling reduces the local thermal gradient and the rate of advance of the tip. As the process continues "equilibrium" is reached between this growth and retardation forcing and the tip advance approaches a steady-state velocity. For a given under-cooling and value of ($\gamma\theta$) the steady-state tip velocity can be predicted from the so called "microscopic solvability theory", see Udaykumar et al. [12] for a compact discussion. Fig. 5 plots the change of dimensionless tip velocity with time for the growth of the equiaxed crystal shown in Fig. 4; the velocity for the grid sizes of 4, 3.25, and 2.5 are reported. This result clearly shows that the enthalpy predicted tip velocity does approach the steady-state microscopic solvability velocity, the solid line in Fig. 5 (taken form Ref. [16]). The result also confirms the small grid dependence, across the chosen range, illustrated in the time snap shot of Fig. 4. It is noted, however, that if smaller grid sizes are used the predicted tip velocity slips below the microscopic solvability limit. This is attributed to the "narrow band" problem [31] discussed above and indicates that the smearing remedial scheme proposed to elevate this problem may only work across a range of grid sizes. Essentially, even with a smearing remedial scheme in place, the choice of too fine a grid size may lead to a poor estimate of the curvature.

5.5. Grid anisotropy

A critical problem with any fixed grid method is grid anisotropy where the layout and design of the grid influences the preferred growth direction. Indeed early [22,23] and some recent enthalpy models [6,25] rely on the grid to promote the preferred growth direction of the crystal. In the current work the preferred growth direction is controlled through the specification of the anisotropic surface energy in (20). Grid anisotropy, however, may still be present in the predicted results. The level of grid anisotropy can be quantified by two tests. In the first test, the run of Fig. 4 is repeated setting the anisotropic strength term in (20) to $\varepsilon = 0$. With this setting the initial seed should grow into and maintain the shape of a circle. Fig. 6 shows the prediction of the crystal at dimensionless $t = 6000$ and space step $\Delta = 4$, under this condition; the prediction of the close to circular shape indicates a low grid anisotropy.

The second test for grid anisotropy is more stringent. The run of Fig. 4 with $\Delta = 2.5$ is repeated using a anisotropic capillary length defined by

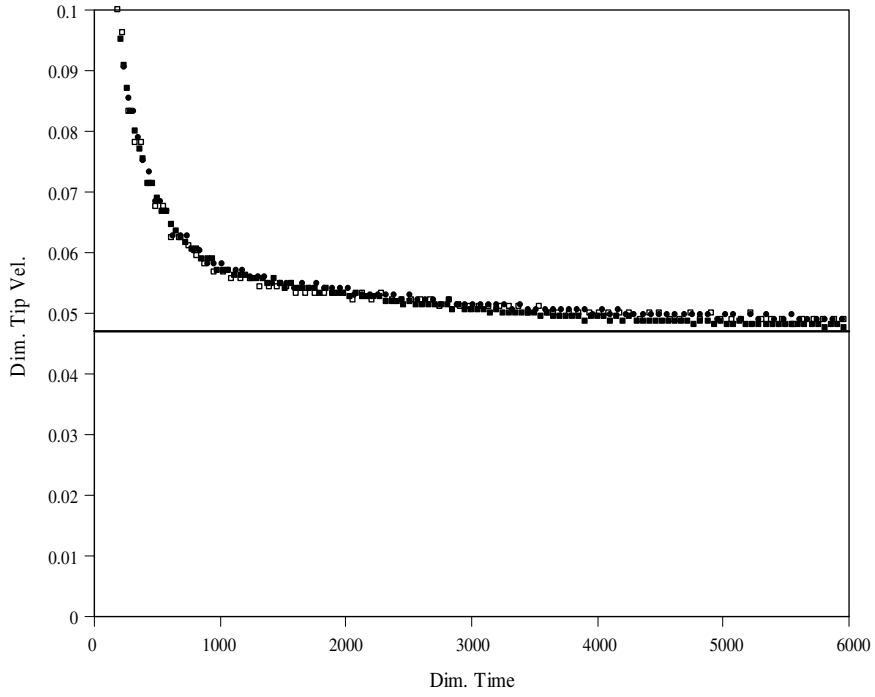

Fig. 5. Dimensionless tip velocity with time for grids of $\Delta = 4$, 3.75 and 2.5; conditions as in Fig. 4.

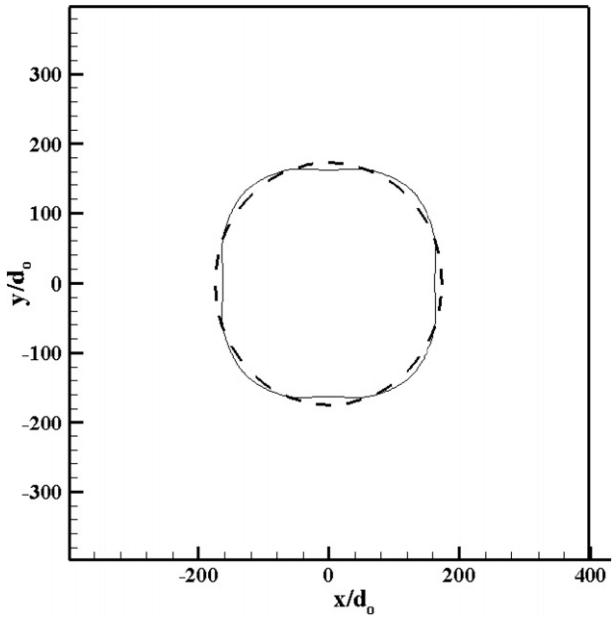

Fig. 6. Growth with zero anisotropic strength $\varepsilon = 0$; all other conditions as in Fig. 4; dashed line theoretical circle, solid crystal prediction.

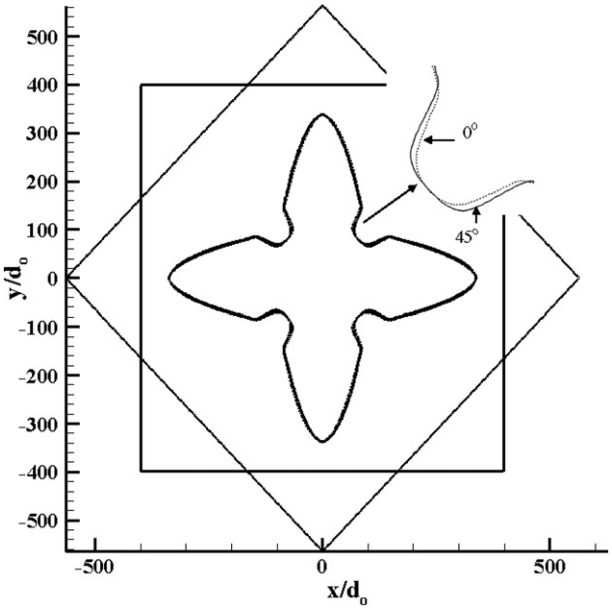

Fig. 7. Comparison between dendrite predictions, dashed line preferred growth alighted with grid, full line preferred growth at 45° to the grid. $\Delta = 2.5$. Conditions as in Fig. 4 with the exception of a setting of $\beta = 0.05$ for the 45° case.

$$d(\theta) = d_0(1 - 15\varepsilon\cos 4(\theta + \pi/4)) \tag{33}$$

with the anisotropic strength reset to $\varepsilon = 0.05$. In this case the same fourfold symmetry crystal will grow, but its arms will be aligned at an angle of 45° to the direction of the finite difference grid. The predicted result, crystal shape at time $t = 6000$, is reported in Fig. 7 by twisting the results through 45° and comparing with the original shape prediction of Fig. 4. The comparison, for the case shown, is excellent. Note, however, that in Fig. 7 the smear parameter in (39) is $\beta = 0.05$ as opposed to the value of $\beta = 0.25$ used when the preferred growth is aligned with the grid.

6. Results

Following the verification of the proposed enthalpy method for dendritic growth a number of results are presented.

6.1. A binary alloy

The growth of a crystal in a binary alloy is simulated, the settings are surface anisotropic strength $\varepsilon = 0.02$, initial under-cooling $T_u = -0.55$, partition coefficient $k = 0.15$, $MC_0 = 0.1$ and a Lewis number $Le = 20$. A grid size of $\Delta = 2.5$ is used in a 1/4 box of 160×160, calculations are carried out to time $t = 30{,}000$. Fig. 8 shows the predicted dendritic shape and the liquid concentration contours; the insert to the right shows the concentration profiles along the x-axis and the line $x = y$. Consistent with the one-dimensional analytical solution there is only limited micro-segregation in the solid and, as indicated by the concentration profiles along $x = 0$ and $y = x$ (see insert), significant solute "pile up" at the solid–liquid interface. The insert to the left shows shape predictions with $Le = 100$ (a number approaching metal alloys) at $t = 50{,}000$ and $\Delta = 1.875$.

The effect of Lewis number is further shown by the series of predicted dendrite shapes in Fig. 9. In this prediction the settings are identical to those used in Fig. 4, with the addition of a non-zero partition number $k = 0.15$. In this figure the simulation time $t = 6000$, is identical for each dendrite; the size and shape is controlled by the Lewis number. If the Lewis number is large, as seen in metal systems, the concentration boundary layer is thin, resulting in a solute pileup along the solid–liquid interface, a low interface under-cooling, and a slower growth. When the Lewis number approaches zero, arrived at by increasing the liquid diffusivity, any solute rejected on solidification is rapidly carried away into the bulk and growth approaches that seen in the pure material case of Fig. 4.

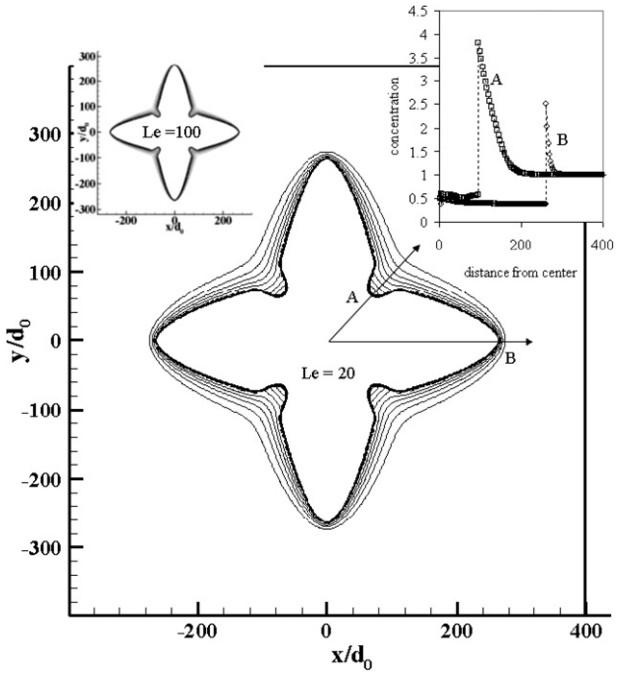

Fig. 8. Dendritic growth in a binary alloy, concentration contours in liquid and concentration profiles along (A) $y = x$ and (B) $x = 0$ at dimensionless time $t = 30{,}000$. Conditions, $\varepsilon = 0.02$, $T_u = -0.55$, $k = 0.15$, $Le = 20$, $\Delta = 2.5$ is used in a 1/4 box of 160×160. Insert shows results for $Le = 100$ at $t = 50{,}000$ with $\Delta = 1.875$.

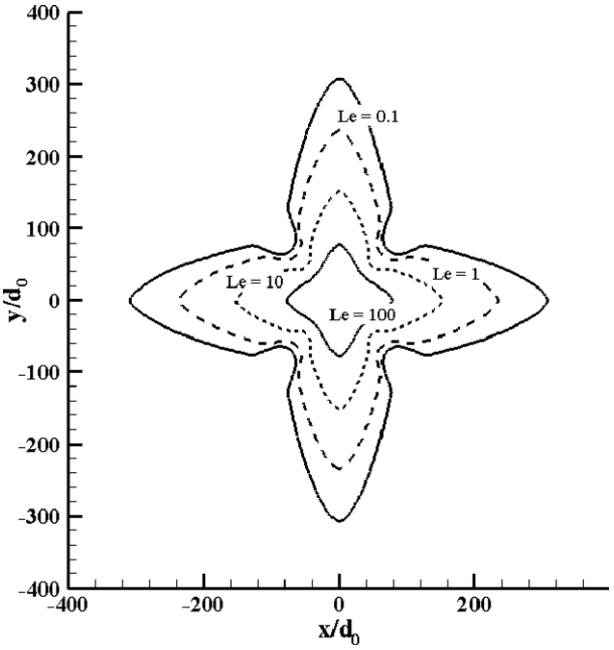

Fig. 9. Dendritic solidification in an alloy effect of Lewis number on shape at time $t = 6000$. Conditions as in Fig. 4 but with partition $k = 0.15$ and $MC_0 = 0.1$. $\Delta = 3.333$ ($Le = 0.1$, 1, 10 and 100) $\Delta = 2$ ($Le = 100$). Time step is chosen so that $\Delta t = 0.1 Le \Delta^2$ (while $Le < 1$) or $\Delta t = 0.1\Delta^2$ otherwise.

6.2. Secondary arms

To obtain secondary arms noise needs to be introduced into the calculation. Following Pal et al. [6] thermal noise can be introduced by allowing for random fluctuations in dimensionless latent heat, i.e., use the spatial field

$$\Delta H(x,y) = (1 + \lambda \mathrm{RND}(x,y)) \tag{34}$$

where $\mathrm{RND}(x,y)$ is a random number in $[0,1]$, the function is symmetric, $\mathrm{RND}(x,y) = \mathrm{RND}(y,x)$, and $\lambda < 1$ is a scaling. Fig. 10 shows the calculated dendrite shape at dimensionless time $t = 12{,}000$, the settings are as in Fig. 4 but with a lower under-cooling $T_u = -0.7$. The noise scaling is set at $\lambda = 0.1$ and a step size of $\Delta = 4$ in a 1/4 box of 1200×1200 is used. The plot in Fig. 10 clearly shows the initiation and growth of secondary arms.

6.3. Grain growth

The proposed method can be used to model the growth of multiple grains. This is achieved by using a full box simulation 800×800 and imposing periodic conditions. In the simulation presented, in Fig. 11, five grains are seeded in the initially under-cooled melt, each with a different preferred growth direction. In a full box the directional smearing of the liquid fraction fields used to calculate the curvature (28) needs to be replaced by the more general

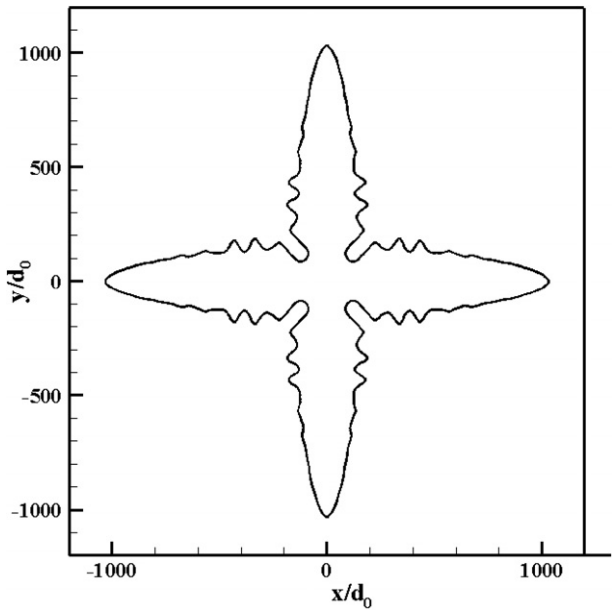

Fig. 10. Inception of secondary arms from thermal noise at time $t = 12{,}000$. Settings as Fig. 4 but with $T_u = -0.7$ and a thermal noise scaling in (34) of $\lambda = 0.1$.

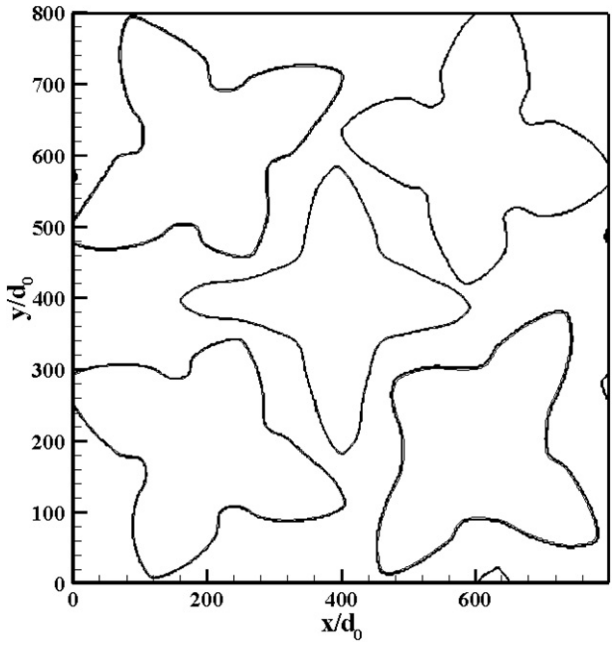

Fig. 11. Simulation of grain growth at time $t = 4000$ with $\Delta = 2.5$. Basic conditions as in Fig. 4 but a full box (800×800) domain is used and smearing function is (38) with $\beta = 0.1$.

approach of (27); a setting of $\beta = 0.1$ is used. The grains at time $t = 4{,}000$ clearly show that the competition between the grains modifies the growth and shape of the dendrite arms.

6.4. CPU

The proposed method can produce sound predictions within very limited CPU time. On a modest windows based lap top the prediction of the $\Delta = 4$ dendrite in Fig. 4 takes on the order of 1 minute of CPU time. Calculations with binary alloys and large Lewis number (e.g., Fig. 8), can take 1–3 h.

7. Conclusions

A fixed grid enthalpy like method has been developed for the simulation of dendritic growth in an under-cooled binary alloy melt. This is the first time that an enthalpy method has been used to model dendritic growth in a binary alloy with explicitly imposed crystal anisotropy. In the development of the method care has been taken to fully verify the proposed approach and point out and explain potential deficiencies. In basic operation the proposed approach can predict dendrite shapes that are consistent with previous results, approach the correct – theoretical – steady-state behavior, show reasonable grid independence, and are relatively free of grid anisotropy. The method can be readily extended to account for binary alloys and the presence of multiple grains. A potential weakness in the method is the loss of resolution is calculating interface curvatures when the grid size decreases below the size of the expected tip radius. Mechanisms that smear out the liquid fraction field in the calculation of interface curvature will reduce this problem. A real strength of the method is its low computer cost released through the explicit scheme time integration and limiting iterations to the narrow band of nodes in the phase change region. This feature allows the proposed method to predict physically feasible dendritic morphologies for a very modest computer cost.

Further work will focus on refining the curvature calculations and accounting for additional phenomena, e.g., effects of electromagnetic fields. Closely related work is also underway to adopt the enthalpy method developed here to handle problems where an under-cooling is not applied but develops, as a result of constitutional under-cooling, during the solidification, see Ref. [32].

Acknowledgements

The authors would like to acknowledge Georgi Djambazov of the University of Greenwich, London for very useful and time saving suggestions for the reordering of the closure iterations. The referees also provided useful guidance that improved the paper.

References

[1] Y.H. Shin, C.P. Hong, Modeling of dendritic growth with convection using a modified cellular automaton model with a diffuse interface, ISIJ Int. 42 (2002) 359–367.
[2] M. Plapp, A. Karma, Multiscale finite-difference-diffusion-monte-carlo method for simulating dendritic solidification, J. Comput. Phys. 165 (2000) 592–619.
[3] C. Beckermann, H.-J. Diepers, I. Steinbach, A. Karma, X. Tong, Modeling melt convection in phase-field simulations of solidification, J. Comput. Phys. 154 (1999) 468–496.

[4] J.-H. Jeong, N. Goldenfeld, J.A. Dantzig, Phase field model for three-dimensional dendritic growth with fluid flow, Phys. Rev. E 64 (2001) 041602.
[5] H.S. Udaykumar, S. Marella, S. Krishnan, Sharp-interface simulation of dendritic growth with convection: benchmarks, Int. J. Heat Mass Transfer 46 (2003) 2615–2627.
[6] D. Pal, J. Bhattacharya, P. Dutta, S. Chakraborty, An enthalpy model for simulation of dendritic growth, Numer. Heat Transfer B 50 (2006) 59–78.
[7] J.C. Ramirez, C. Beckermann, A. Karma, H.-J. Diepers, Phase-field modeling of binary alloy solidification with coupled heat and solute diffusion, Phys. Rev. E 69 (2004).
[8] P. Zhao, M. Vénere, J.C. Heinrich, D.R. Poirier, Modeling dendritic growth of a binary alloy, J. Comput. Phys. 188 (2003) 434–461.
[9] V.R. Voller, An enthalpy based scheme for simulating dendritic growth, in: C.A. Gandin, M. Bellet (Eds.), Modeling of Casting, Welding and Advanced Solidification Processes-XI, TMS, Warrendale, PA, 2006, pp. 465–472.
[10] J.M. Sullivan Jr., D.R. Lynch, Finite element simulation of planar instabilities during solidification of an undercooled melt, J. Comput. Phys. 69 (1987) 81–111.
[11] H.S. Udaykumar, R. Mittal, W. Shyy, Computation of solid–liquid phase fronts in the sharp interface limit on fixed grids, J. Comput. Phys. 153 (1999) 535–574.
[12] H.S. Udaykumar, L. Mao, R. Mittal, A finite-volume sharp interface scheme for dendritic growth simulations: comparison with microscopic solvability theory, Numer. Heat Transfer B 42 (2002) 389–409.
[13] J.P. Zhao, J.C. Heinrich, Front-tracking finite element method for dendritic solidification, J. Comput. Phys. 173 (2001) 765–796.
[14] D. Juric, G. Tryggvason, A front tracking method fro dendritic solidification, J. Comp. Phys. 123 (1996) 127–148.
[15] S. Chen, B. Merriman, S. Osher, P. Smereka, A simple level set method for solving Stefan problems, J. Comp. Phys. 135 (1997) 8–29.
[16] Y.-T. Kim, N. Goldenfeld, J. Dantzig, Computation of dendritic microstructures using a level set method, Phys. Rev. E 62 (2000) 2471–2474.
[17] A. Karma, W.-J. Rappel, Quantitative phase-field modeling of dendritic growth in two and three dimensions, Phys. Rev. E 57 (1998) 4323–4349.
[18] N. Provatas, N. Goldenfeld, J. Dantzig, Adaptive mesh refinement computation of solidification microstructures using dynamic data structures, J. Comp. Phys. 148 (1999) 265–279.
[19] W.D. Boettinger, J.A. Warren, C. Beckermann, A. Karma, Phase-field simulations of solidification, Annu. Rev. Mater. Res. 32 (2002) 163–194.
[20] L. Tan, N. Zabaras, A level set simulation of dendritic solidification with combined features of front-tracking and fixed-domain methods, J. Comput. Phys. 211 (2006) 36–63.
[21] Y. Sun, C. Beckermann, Sharp interface tracking using the phase-field equation, J. Comput. Phys. 220 (2006) 626–653.
[22] K.-H. Tacke, in: K.-H. Hofmann, J. Sprekels (Eds.), Application of finite difference enthalpy methods to dendritic growth, free boundary problems: theory and applications, Longman Sci. Tech., Essex, 1990.
[23] K.-H. Tacke, A. Harnisch, Finite difference enthalpy methods for dendritic growth, Proceedings of the International Conference on Computational Modeling of Free and Moving Boundary Problems, WIT press, Southampton, 1991.
[24] V.R. Voller, N. Murfield, Application of an enthalpy method for dendritic solidification, in: A.J. Nowak et al. (Eds.), Numerical Heat Transfer 2005, Institute of Thermal Technology, Poland, 2005, pp. 379–386.
[25] D. Chatterjee, S. Chakraborty, A hybrid lattice boltzmann model for solid–liquid phase transition in presence of fluid flow, Phys. Lett. A 351 (2006) 359–367.
[26] V.R. Voller, Numerical methods for phase-change problems, in: W.J. Minkowycz et al. (Eds.), Handbook of Numerical Heat Transfer, John Wiley, New York, 2006, Chapter 19.
[27] J. Crank, Free and Moving Boundary Problems, Claredon Press, Oxford, 1984.
[28] A.B. Crowley, J.R. Ockendon, On the numerical solution of an alloy solidification problem, Int. J. Heat Mass Transfer 22 (1979) 941–947.
[29] J.A. Sethian, Level Set Methods and Fast Marching Methods, Cambridge University Press, 1999.
[30] V.R. Voller, A similarity solution for solidification of an under-cooled binary alloy, Int. J. Heat Mass Transfer 49 (2006) 1981–1985.
[31] S. Cummins, M. Francois, D. Kothe, Estimating curvature from volume fraction, Comput. Struct. 83 (2005) 425–434.
[32] V.R. Voller, A numerical method for the Rubinstein binary-alloy problem in the presence of an under-cooled liquid, Int. J Heat Mass Transfer 51 (2008) 696–706.